# Lithium halide coating as an effective intergrain engineering for garnet-type solid electrolytes avoiding high temperature sintering

Zhang, Zhaoshuai; Zhang, Long; Yu, Chuang; Yan, Xinlin; Xu, Bo; Wang, Li min

**DOI**
10.1016/j.electacta.2018.08.079

**Publication date**
2018

**Document Version**
Accepted author manuscript

**Published in**
Electrochimica Acta

Contents lists available at ScienceDirect

Electrochimica Acta

journal homepage: www.elsevier.com

# Lithium halide coating as an effective intergrain engineering for garnet-type solid electrolytes avoiding high temperature sintering

Zhaoshuai Zhang[a], Long Zhang[a, *], Chuang Yu[b], Xinlin Yan[c], Bo Xu[a], Li-min Wang[a]

[a] State Key Laboratory of Metastable Materials Science and Technology, Yanshan University, Qinhuangdao, Hebei, 066004, China
[b] Department of Radiation Science and Technology, Delft University of Technology, Mekelweg 15, Delft, 2629 JB, The Netherlands
[c] Institute of Solid State Physics, Vienna University of Technology, Wiedner Hauptstr. 8-10, 1040, Vienna, Austria

ARTICLE INFO

*Article history:*
Received 20 April 2018
Received in revised form 28 June 2018
Accepted 28 August 2018
Available online xxx

*Keywords:*
$Li_7La_3Zr_2O_{12}$
Garnet
Lithium halides
Coating
Solid electrolytes

ABSTRACT

Garnet-type $Li_7La_3Zr_2O_{12}$ solid electrolytes were commonly prepared by two steps solid-state reaction method, which undergoes high temperature over 1000 °C and thus inevitable for lithium volatilization and formation of secondary phases. Here, we propose a new intergrain architecture engineering of a solution method, to avoid high temperature sintering for preparing lithium halide (LiX) coated garnet-type solid electrolytes, which contain Al and Ta co-doped $Li_7La_3Zr_2O_{12}$ ($Li_{6.75}La_3Zr_{1.75}Ta_{0.25}O_{12}$, LLZTO) synthesized at 900 °C with cubic structure. Owing to the increased relative density, the improved formability, and the altered ion transport mode from point to face conduction by LiX coating on LLZTO grains, LiX-coated LLZTO samples demonstrate a good Li dendrite suppression ability and a high ionic conductivity that is three orders of magnitude higher than pristine LLZTO. In another way, this result demonstrates the critical role of the grain boundaries on the ion transport for oxide superionic conductors. The present coating method provides a new strategy to prepare brittle solid electrolytes avoiding high temperature sintering.



## 1. Introduction

Next generation lithium-ion batteries (LIBs) with high energy density, high capacity as well as high safety are in strong demand for uses in portable devices, electrical vehicles, and large-scale energy storage systems [1–3]. The safety risk especially associated with the flammable organic liquid electrolytes becomes a serious concern for next generation LIBs. One of the primary strategies to solve the safety issue is to develop all-solid-state batteries based on solid electrolytes (SEs, also known as solid-state superionic conductors). The substitution of organic liquid electrolytes by SEs raises several advantages including: non-inflammability, absence of leakage, and good thermal stability. Additionally, direct stacking of all-solid-state batteries leads to high operating voltages and volumetric energy density, both of which are ideal for vehicle applications [4–7].

Among various inorganic superionic conductors, the garnet-type $Li_7La_3Zr_2O_{12}$ (LLZO), discovered by Thangadurai and Weppner in 2007 [8], is one of the most promising solid electrolytes because of its high chemical stability, wide potential window, and relatively high ionic conductivity at room temperature [9–13]. Generally, a cubic structure and a good contact between grains are prerequisites for maintaining a high ionic conductivity of LLZO [14]. Although tetragonal structure ($I4_1/acd$, No. 142) [15] is easy to be stabilized at room temperature for LLZO, it shows a lower ionic conductivity compared to the cubic structure ($Ia$-3d, No. 230) [16]. Doping with Al, Nb, Ta, Ga, etc. to create vacancies and sintering over 1000 °C are effective ways commonly used to stabilize cubic LLZO at room temperature [17,18].

High temperature sintering over 1100 °C is also adopted to get high density samples with tight grain boundaries, and thus a low grain boundary resistance. However, these two steps high temperature sintering processes give rise to Li volatilization, i.e., the compositional deviation, which leads to a low ionic conductivity. To build an all-solid-state battery based on LLZO solid electrolyte, a high interfacial resistance on the solid electrolyte/electrode interface is the key issue [19]. High temperature sintering used to solve this issue is difficult because the diffusion reaction between electrolyte and electrode results in a high impedance at the solid interface and an intensive deterioration in the battery performance [2,4,20]. Developing a new technique to avoid high temperature sintering for LLZO preparation is highly anticipated.

Kähäri et al. proposed a low temperature sintering technique based on solution method in 2014 [21]. Compared to the samples sintered at high temperatures, the sample prepared at low temperatures (through evaporating the solvent) shows the similar microstructure, density, and dielectric properties. Very recently, Randall et al. demonstrated that many inorganic materials and ceramic-based composites can be sintered at low temperatures through a solution method by using either an acidic or a basic aqueous solution [22]. $Li_{1.5}Al_{0.5}Ge_{1.5}(PO_4)_3$ (LAGP) with a density of 80% was prepared by this method below 160 °C [23]. However, a pressure of 400 MPa was applied during heat treatment. A hot press sintering process increases the cost and is not compatible to current battery fabrication tech-

* Corresponding author.
*Email address:* lzhang@ysu.edu.cn (L. Zhang)

https://doi.org/10.1016/j.electacta.2018.08.079
0013-4686/ 

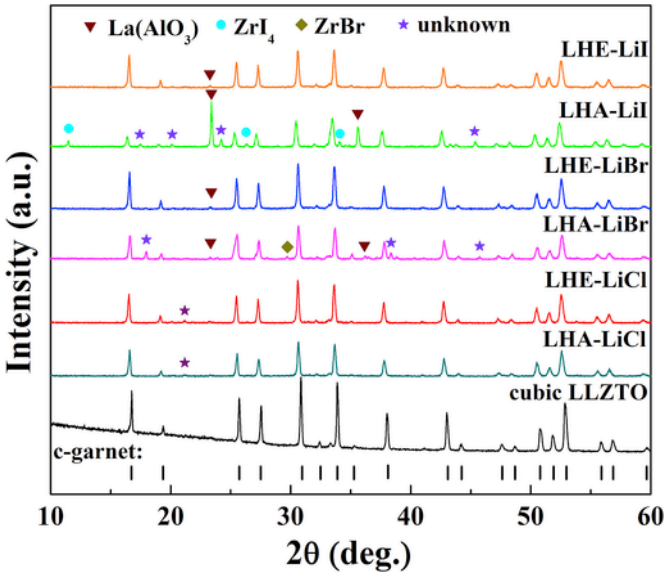


**Fig. 1.** XRD patterns of pristine LLZTO and LiX-coated LLZTO. The corresponding Bragg positions to phases are marked.

niques. Additionally, the ionic conductivity is less than $10^{-5}$ S/cm and the electrochemical stability data is absent in that paper [23]. On the other hand, introducing the liquid phase at the particle-particle interfaces is also an useful way to minimize the interfacial resistance between LLZO particles [12,24,25], though a small amount of liquid is presented. In general, these works open a new route to assemble all-solid-state batteries to avoid the side effects induced by high temperature sintering.

In this work, we successfully synthesized Al and Ta co-doped LLZO with cubic structure at 900 °C. More importantly, we designed a new type of hybrid garnet solid electrolytes containing LLZTO ($Li_{6.75}La_3Zr_{1.75}Ta_{0.25}O_{12}$) ceramic powders coated by LiX (X=Cl, Br, I) using solution method without pressure loading. The LLZTO powders were uniformly wetted with an appropriate amount of LiX ethanol or an aqueous solution. Solid-state LiX-coated LLZTO was formed after evaporating the solvent at 160 °C. LiX with different halogens and its coating concentration were optimized. LiCl-coated LLZTO demonstrates a high relative density benefited from the filling of LiCl in the pores between grains, and thus achieving a high ionic conductivity and a good Li dendrite suppression ability. LiCl-coated LLZTO prepared by the solution method possesses comparable good performance to those sintered under high temperature.

## 2. Experimental section

### *2.1. Synthesis of cubic LLZTO*

Cubic LLZTO was synthesized by conventional solid-state reaction. The starting materials $Li_2CO_3$ (Aladdin reagent, 99.99%), $La_2O_3$ (Aladdin reagent, 99.99%), $ZrO_2$ (Aladdin reagent, 99.99%), $TaCl_5$ (J&K Chemical, 99.99%) and $Al_2O_3$ (Aladdin reagent, 99.99%) powders were weighed and mixed in stoichiometric amounts with the molar ratio of Li:La:Zr:Ta to be 6.75:3:1.75:0.25. A proper amount of $Al_2O_3$ was added to obtain a doping level of 0.24 mol of Al in one unit formula of garnet. A 10 wt% excess of $Li_2CO_3$ was used to compensate Li volatilization during synthesis. The mixed powders were placed in a tungsten carbide vial and ball-milled in Ar

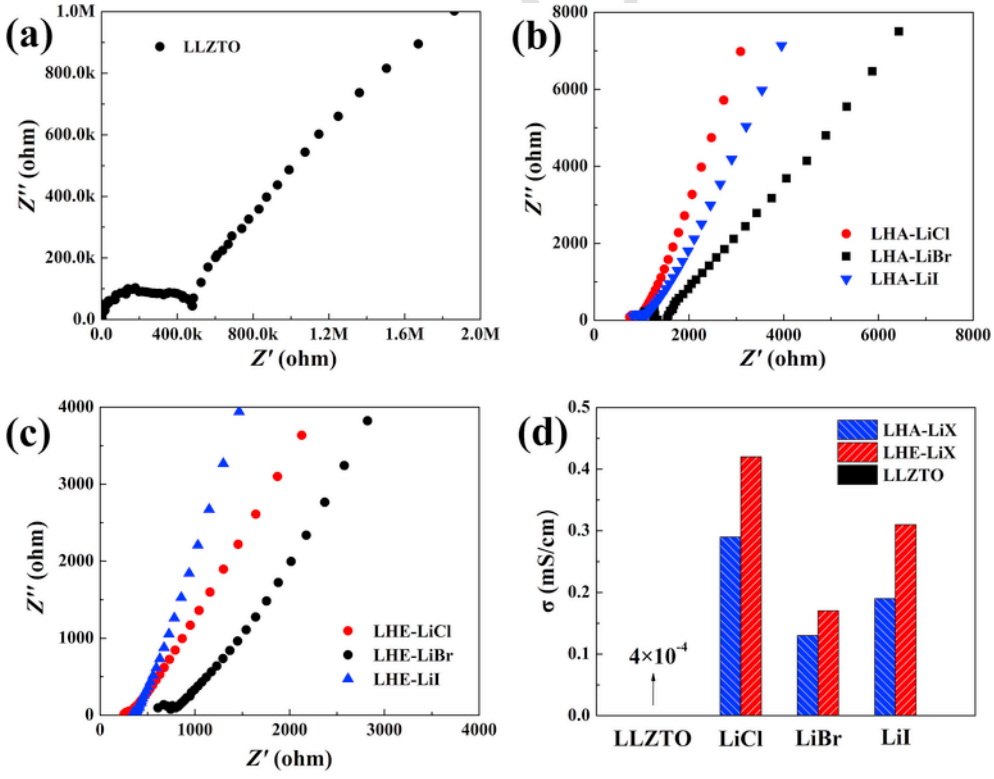


**Fig. 2.** Impedance spectra measured at room temperature for: (a) pristine cubic LLZTO, (b) LHA-LiX, and (c) LHE-LiX. (d) Ionic conductivity histogram of pristine LLZTO and LiX-coated LLZTO. Note: X=Cl, Br, I.

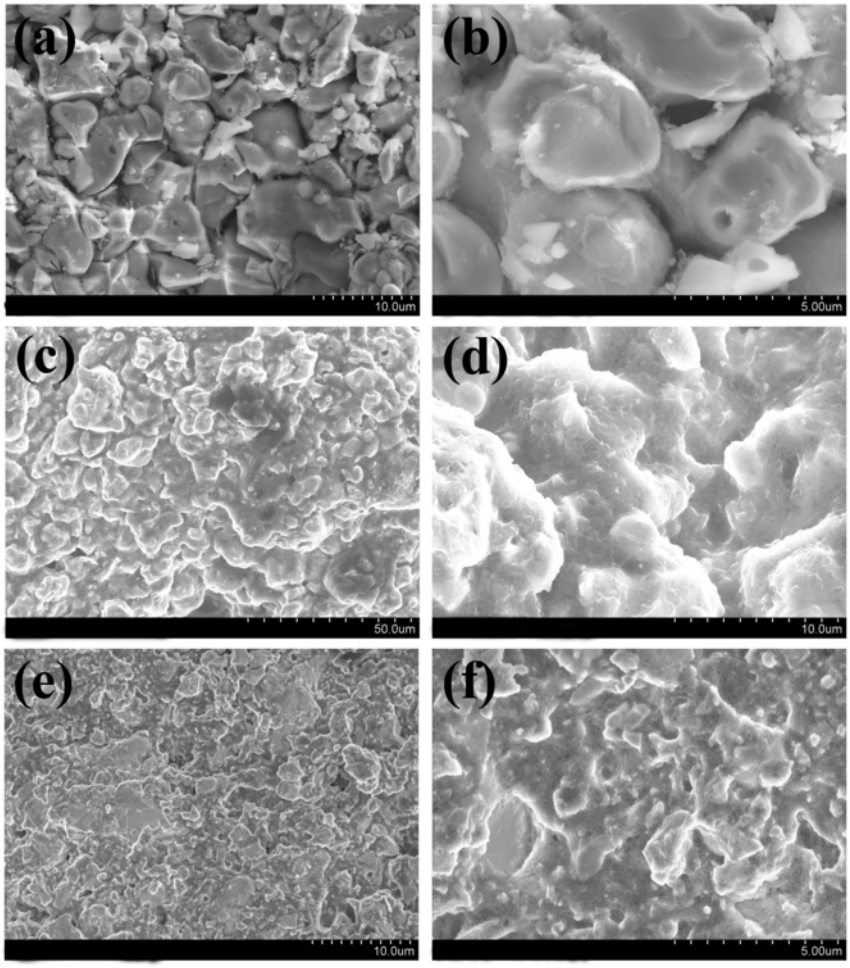


**Fig. 3.** The cross-section SEM images of pristine LLZTO (a,b), LHA-LiCl (c,d) and LHE-LiCl (e,f).

atmosphere for 8 h with a rotational speed of 150 rpm. The resulting mixture was heated in air atmosphere at 900 °C for 5 h in an alumina crucible with a heating rate of 2.5 °C/min. The sintered powders were then ball-milled for 2 h to refine the particle size. The resulting LLZTO powders were finally sieved using a 45 μm mesh.

### *2.2. Preparation of solid-state LiX-coated LLZTO*

Anhydrous LiCl (Alfa Aesar, 99%), anhydrous LiBr (Alfa Aesar, 99%) or anhydrous LiI (Alfa Aesar, 99%) powders were dissolved in deionized water or anhydrous ethanol to form aqueous or ethanol solutions with a concentration of 2 mol/L. For optimization of the LiX solutes and solvents, the weight ratio of LLZTO powders to LiX solutions (aqueous or ethanol solution) was fixed to 96:4. The well dissolved LiX aqueous solution or LiX ethanol solution was evenly sprayed onto the pristine LLZTO powders. The control experiments with pure solvents (water or ethanol) sprayed LLZTO were prepared under the same conditions. The wetted powders were collected and pressed under an axial pressure of ~10 MPa to form a pellet about 1 mm thickness. The pellets were then placed in a vacuum oven heated at 160 °C for 12 h to evaporate the solvent (aqueous or ethanol). For convenience, the LiX-coated LLZTO samples prepared from aqueous solutions are named as LHA-LiX and those prepared from ethanol solutions are named as LHE-LiX, where X = Cl, Br, and I; The optimized LHE-LiCl sample with 6 wt% LiCl ethanol solution is named as LHE-LiCl-LLZTO, which is used for the characterization of structural, thermal, and electrochemical properties. As a comparison, the pristine LLZTO powders were also pressed under a higher pressure of 350 MPa. All preparations were handled in a glove box (Mikrouna, China) filled with high purity Ar.

### *2.3. Materials characterization*

X-ray powder diffraction (XRD) was performed using a Rigaku D/MAX-2500/PC (Cu K$\alpha$, 40 kV 200 mA) in the range of 2θ = 10–60° with a step size of 0.02°. Fracture images and chemical compositions were measured using a Hitachi S-4800 II FESEM equipped with an energy dispersive spectrometry (EDS). Raman scattering measurements were performed using a Renishaw inVia system with a 532 nm excitation source. Thermogravimetric analysis (TGA) measurements were carried out on a Netzsch STA thermoanalyzer from 50 to 350 °C with a heating rate of 5 °C/min in Ar atmosphere.

### *2.4. Electrochemical characterization*

Electrochemical Impedance Spectroscopy (EIS) measurements were performed using a Princeton P4000 impedance analyser in the frequency range of 0.1 Hz–5 MHz at room temperature. Two sides of the pellets for measurements were polished and coated by Au [26]. Samples were assembled in an Ar-filled glove box to avoid moisture

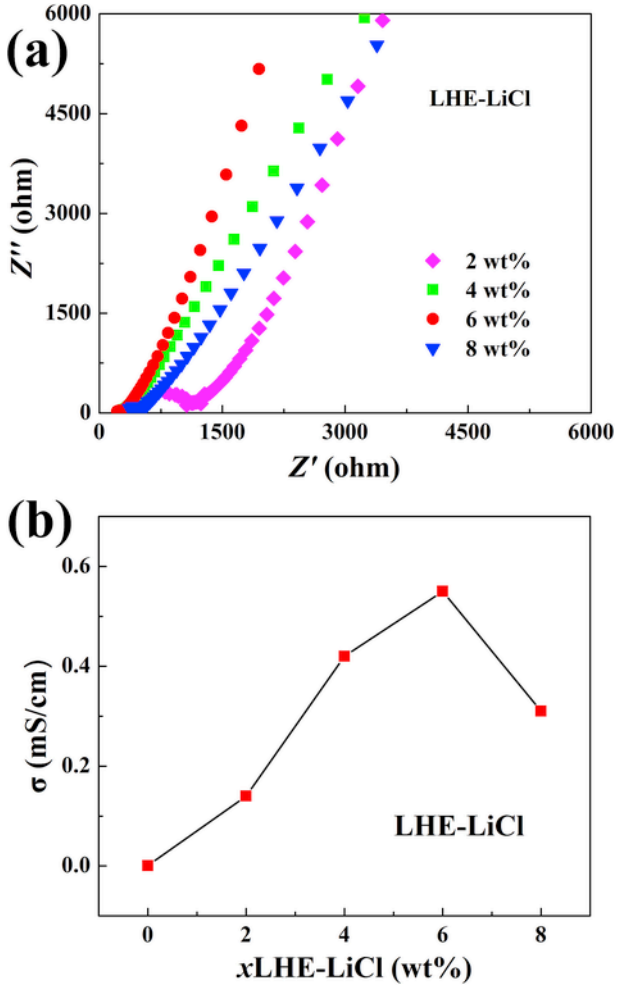


**Fig. 4.** (a) Impedance spectra for various LiCl-coated samples. (b) Ionic conductivity as a function of LiCl coating. The weight ratio was calculated from the weight of LiCl ethanol solution compared to the total weight of the sprayed LLZTO powders.

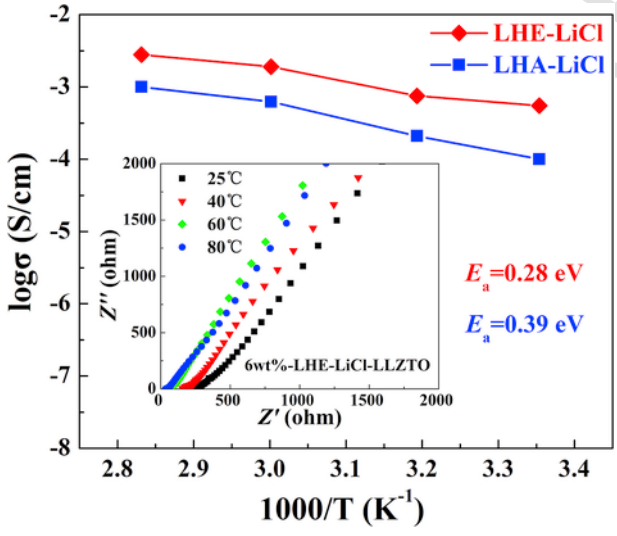


**Fig. 5.** Arrhenius conductivity plots of LiCl-coated LLZTO solid electrolytes prepared from ethanol- and aqueous-based solutions.

contamination [27]. Li/LHE-LiCl-LLZTO/Li and Li/PCL/LHE-LiCl-LLZTO/PCL/Li symmetric cells were cycled at a constant current density of 0.1 mA/cm$^2$. The detailed preparation of PCL (polycaprolactone) films (nonuse of fiber skeleton) can refer to Ref [28].

$LiFePO_4$/LHE-LiCl-LLZTO/Li cell was fabricated as following. The cathode was prepared by mixing 80 wt % $LiFePO_4$ active materials, 10 wt % carbon black, and 10 wt % Poly(vinylidene fluoride) (PVDF), dissolved in N-methylpyrrolidinone (NMP). The resulting slurry was pasted onto carbon-coated aluminum foil and dried at 100 °C for 12 h under vacuum. The mass loading of the active material ($LiFePO_4$) on the electrodes is ~1.5 mg/cm$^2$. The cathode, LHE-LiCl-LLZTO solid electrolyte, and Li foil were assembled into a CR2032 coin cell. Approximately 12 μL commercial liquid electrolyte was added to the cathode side to reduce the interfacial resistance of cathode/electrolyte [29]. Liquid electrolyte is only wetted the interface but not deeply permeates into the solid electrolyte, and thus not affecting the solid electrolyte. The liquid electrolyte is a $LiPF_6$-dissolved carbonate-based electrolyte, purchased from Kejingstar LTD. with a code of LBC305-1. The charged and discharged tests were performed at a current density of 0.03 mA/cm$^2$ between 2.55 and 4.2 V at ambient temperature (16 °C).

## 3. Results and discussion

### *3.1. Optimization of LiX-LLZTO*

XRD patterns for pristine LLZTO and different LiX-coated LLZTO samples are shown in Fig. 1. For these samples, the weight ratio of LLZTO powders to LiX solutions (aqueous or ethanol solution) was fixed to 96:4. The Bragg positions of the cubic garnet are indexed accordingly. For all LiX-dopted LLZTO, no diffraction peak corresponding to LiX is observed due to the low LiX concentration in the composite. All samples are dominated with cubic garnet structure of *Ia*-3d symmetry, though LiBr- and LiI-coated aqueous-based samples show relatively high impurity phases. Pristine LLZTO and ethanol-based LHE-samples are almost single phase. LHA-LiI shows the highest amount of impurity phases including $La(AlO_3)$, $ZrI_4$, and an unknown phase, indicating a severe decomposition of LLZTO by LiI aqueous solution during the dissolving or evaporating process. Although the impurity amount in LHA-LiBr is significantly lower than that in LHA-LiI, $La(AlO_3)$, ZrBr, and the unknown phase can still be observed. The reason regarding the appearance of impurity phases remains to be further investigated, but it could be related to the different intrinsic behaviors of LiX as shown in LiX-incorporated $Li_2S$-$P_2S_5$ systems [30]. The good stability of garnet in the LiCl solution has been previously reported as well [31–33]. Therefore, it can be concluded that: (1) a negligible chemical reaction takes place between LLZTO and the LiCl solution based on either the aqueous or the ethanol solvent. LiCl is thus preferred for the coating purpose for LLZTO; (2) the chemical stability of LLZTO toward the ethanol solution is much better than that of LLZTO toward the aqueous solution regarding LiBr and LiI solutes. On the other hand, it was reported that the water vapor from atmosphere might enter into the lattice and replace the lithium ions by protons to form O—H bonds, leading to the formation of LiOH with the reaction formulas [34–37]:

$$Li_7La_3Zr_2O_{12} + xCO_2 \rightarrow Li_{7-x}La_3Zr_2O_{12-x} + x{\cdot}Li_2CO_3$$

$$Li_7La_3Zr_2O_{12} + x{\cdot}H_2O \rightarrow Li_{7-x}H_xLa_3Zr_2O_{12} + x{\cdot}LiOH$$

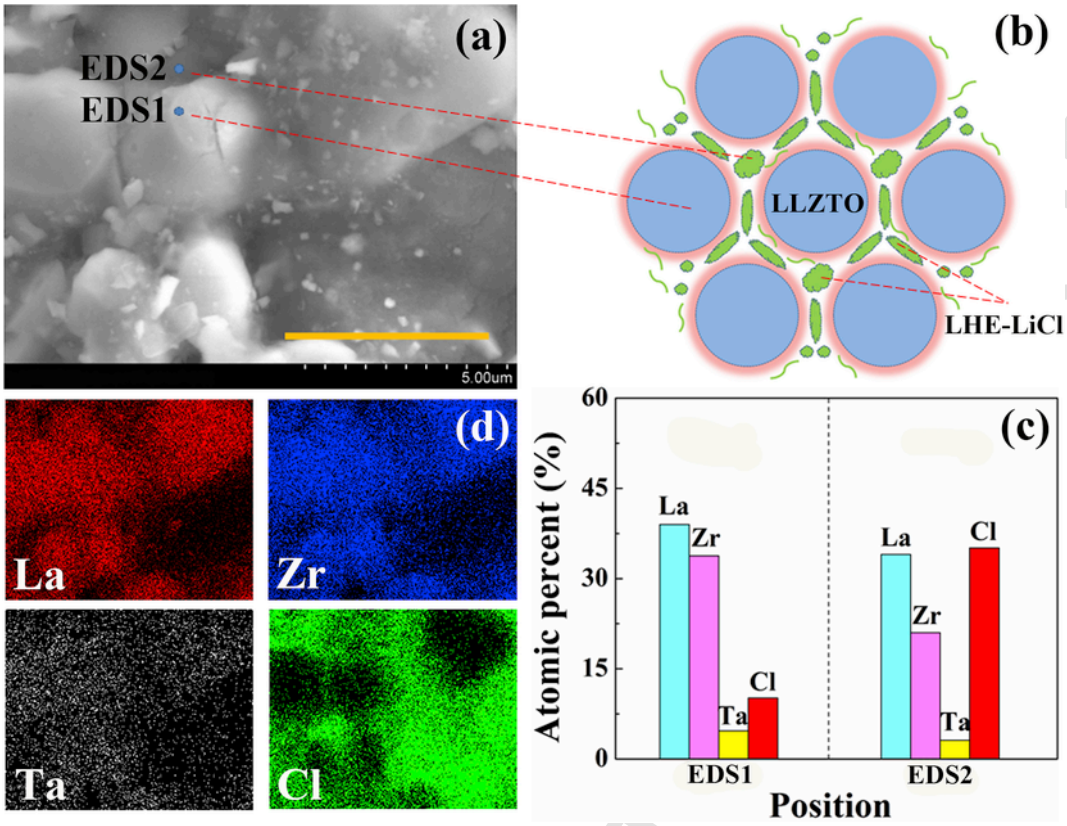


**Fig. 6.** (a) SEM images for the fracture surface of LHE-LiCl-LLZTO. The points marked with EDS1 and EDS2 show the locations for EDS measurements. (b) The schematic illustration of LHE-LiCl-LLZTO solid electrolyte with LLZTO coated by LiCl. (c) The histogram of elemental proportion of La, Zr, Ta, and Cl detected at grains and grain boundaries. (d) EDS mapping of La, Zr, Ta, and Cl in the area corresponding to the fracture image shown in (a).

Although the impurity phases of $Li_2CO_3$ and LiOH are not observed from XRD profiles, they in fact exist with an undetectable small quantity [27].

The ionic conductivity was evaluated for all prepared samples. Fig. 2 displays Nyquist plots of the pristine LLZTO and the LiX-coated LLZTO samples with Au as blocking electrodes at room temperature. The magnification of the high frequency region is shown in Fig. S1. The impedance spectrum of pristine LLZTO (Fig. 2a) shows two semicircles at the high and intermediate frequency spectra, respectively, associated with intragrain and intergrain transport, indicating a large grain boundary resistance. This is in accordance with the results previously reported [24,26,38]. While for all LiX-coated LLZTO samples, the semicircle at intermediate frequency disappears, indicating a small grain boundary resistance and thus a bulk-dominated overall resistance similar to those of sulfide superionic conductors [39,40]. This inherently low grain boundary resistance is expected because LiX coating fills pores on grain boundaries. As a result, the conducting way changes from point contacts to face contacts, which can improve the ion transport between grains. For all samples, a Warburg-type impedance behavior appears at the low frequency region, which can be attributed to a capacitive behavior similar to the blocking electrodes. Such a steep linear spike at low frequency indicates that all LLZTO samples in this work are typical ionic conductors.

Although it is hard to separate the grain and grain boundary contributions, the total resistance can be obtained from the local minimum at the intersection of the impedance plot. The total resistance of the pristine LLZTO is 490 kΩ, two orders of magnitude larger than that of LiX-coated LLZTO. The ethanol-based solution processed samples (Fig. 2c) show lower total resistance than the aqueous-based solution processed samples (Fig. 2b), indicating a better stability of ethanol toward LLZTO. This result is agreement with the XRD result. For different halides, LiBr-coated samples show larger total resistance than LiCl- and LiI-based samples regardless of the solvents. Similar results have been reported that LiX as additives demonstrates various behaviors depending on the electrolytes and the preparation techniques [30,41,42], e.g., LiF and LiCl are preferred to be adopted for oxides [31,43,44] and LiI is preferred to be adopted for sulfides [30,41], though the exact fundamental behind is still unclear so far. The aim of this paper is to propose a new method to reduce the grain boundary resistance of garnet-type solid electrodes. Further investigation is ongoing to elucidate the mechanism of LiX incorporation.

The total ionic conductivity was calculated using the equation $\sigma = L/SR$, where $L$, $R$, and $S$ represent the thickness of LLZTO, the total resistance, and the active area of electrolyte/electrode, respectively. Fig. 2d displays the ionic conductivity histogram of the pristine LLZTO and the LiX-coated LLZTO samples. The ethanol solvent is favorable to a higher ionic conductivity in contrast to the water solvent, though the values are in the same order of magnitude. It is notable that a large amount of impurities in LHA-LiI does not deteriorate the ionic conductivity too much. The ionic conductivity is 0.19 mS/cm for LHA-LiI and 0.31 mS/cm for LHE-LiI. This is reasonable because the impurities are also coated by LiCl, which mitigates the effect of impurities on ion transport. LHE-LiCl achieves the highest ionic conductivity with a value of 0.42 mS/cm at room temperature, which is three orders of magnitude higher than pristine LLZTO ($4 \times 10^{-4}$ mS/cm). Even sintered at 1200 °C to achieve a

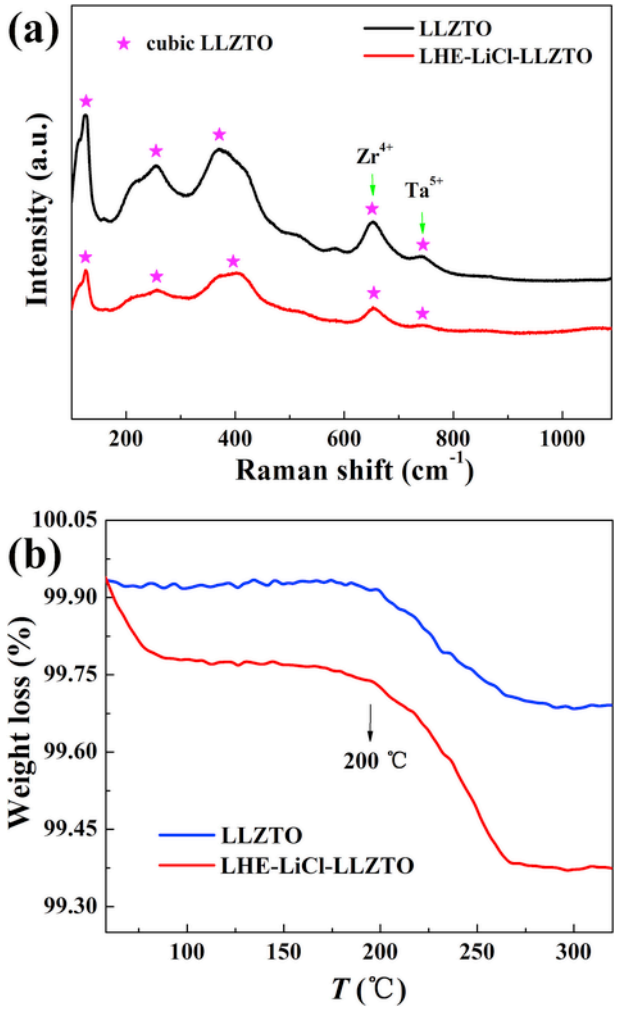


**Fig. 7.** (a) Raman spectra of pristine LLZTO and LHE-LiCl-LLZTO. (b) TG profiles of pristine LLZTO and LHE-LiCl-LLZTO.

highly dense sample (92%, relative density), the ionic conductivity of the pristine LLZTO sample is 0.16 mS/cm (Fig. S2a), which is still lower than the value for most of LiX-coated LLZTO. These results demonstrate the critical role of grain boundary on ion transport for oxide solid electrolytes. LiX coating intensively improves the ion transport by changing the conduction mode from point to face conduction, thus successfully avoiding high temperature sintering on oxide solid electrolytes for well-contact grain boundaries.

Representative cross-sectional images of selected samples are shown in Fig. 3. The samples were fractured and no additional polishing or thermal etching was performed after fracturing. Significant amounts of pores are observed in between the grains for pristine LLZTO (Fig. 3a and b). As a result, it has a low relative density with a value of 67%, resulting in a low ionic conductivity and brittle pellets.

In contrast, the pores were well filled in LiCl-coated samples prepared either from the ethanol solution (Fig. 3c and d) or from the aqueous solution (Fig. 3e and f). The relative density of LiCl-coated samples is ~83%, significantly higher than that of pristine LLZTO. One of the advantages of the solution method is to form a homogenous and thin film layer. Because the thickness of the coating layer is generally a few nanometers, only a trace of coating material is needed [45]. The role of LiX solutions is to form a coating layer on LLZTO powders like a binder. In this case, the volume and the quantity of pores are not as much as those existed in the pellet pressed from solid powders. The homogenous coating layer can be clearly seen from the SEM fracture images with a low magnification (Fig. 3c,e). The effect of LiCl "fillers" formed by low temperature heating is thus analogous to that of fusion between grains under high temperature sintering. As a result, no pore is observed from LiCl-coated LLZTO samples. This is in accordance with the result previously reported that the ceramics can be easily densified with a small fraction of uniformly distributed water [22].

### *3.2. Effect of LiCl concentration on ion transport*

According to the optimized results above-mentioned, LiCl is the best choice among LiX and the ethanol solvent is better than the aqueous solvent. We thus choose the LiCl-ethanol solution as coating precursor and investigate the influence of LiCl coating concentration on the ion transport. Four samples with different weight percentage (2, 4, 6, and 8 wt%) of LiCl ethanol solution were measured. The weight ratio was calculated from the weight of LiCl ethanol solution to the total weight of the sprayed LLZTO powders (the weight of LiCl ethanol solution plus the weight of LLZTO). Fig. 4a shows the Nyquist plots of the impedance for different coating amount of LiCl. The impedance spectra for all samples show an incomplete semicircle in the high frequency region followed by a linear spike in the low-frequency region, indicating typical ionic conductors with negligible grain boundary resistance. The total resistance for all samples is below 1200 Ω. The ionic conductivity was calculated from the total resistance and shown in Fig. 4b as a function of LiCl concentration. The ionic conductivity increases with increasing LiCl concentration, reaches a maximum at 6 wt%, and then decreases. The sample prepared from spraying with 6 wt% LiCl ethanol solution achieves the highest ionic conductivity with a value of 0.56 mS/cm. Since LiCl is

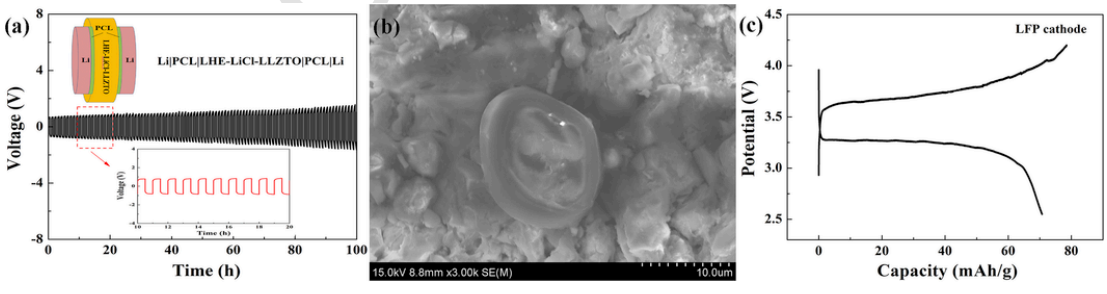


**Fig. 8.** Cyclability of LiCl-coated LLZTO in a symmetric Li/PCL/LHE-LiCl-LLZTO/PCL/Li cell with a current density of 0.1 mA/cm$^2$ at room temperature. (b) Cross-sectional micrograph of the LHE-LiCl-LLZTO electrolyte after polarization test. (c) Charge and discharge curves of the $LiFePO_4$/LHE-LiCl-LLZTO/Li cell at a current density of 0.03 mA/cm$^2$ at ambient temperature (16 °C).

not a good ion conductor [46], the ionic conductivity of LiCl-coated LLZTO is a competition result between pores and LiCl concentration. For a low LiCl concentration (≤6 wt%), LiCl fills the pores and connects the grains to increase the amount of face conduction between grains. The ionic conductivity is thus enhanced with increasing LiCl coating. This mechanism is similar to the effect of $Li_2O$ additives on grain boundary, which enhances the migration of $Li^+$ throughout the ceramics [47]. After the pores are fully filled, the ionic conductivity depends on the thickness of LiCl on grain boundaries. Considering a low ionic conductivity of LiCl, thicker LiCl layer leads to a lower ionic conductivity. The sample prepared from spraying with 6 wt% LiCl ethanol solution (LHE-LiCl-LLZTO) was selected for further investigation.

The control experiments with pure ethanol and water sprayed LLZTO were respectively performed to elucidate the effect of solvent. The corresponding Nyquist plots are shown in Fig. S2b. The grain boundary resistances of these two samples are significantly larger than those of LHA-LiX and LHE-LiX samples. The total ionic conductivities of the former are three orders of magnitude lower than those of the latter. Unlike LiX-coated LLZTO with consecutive coatings, the grain boundaries of water-sprayed LLZTO (Fig. S3) can be clearly seen from the SEM fracture image. The relative densities of pure ethanol (69%) and water (74%) sprayed LLZTO locates in between those of pristine (67%) and LiX-coated LLZTO (83%). LiX not only fills the pores at grain boundaries, but also forms a consecutive layer that submerges grain boundaries. This filling layer may lead to several benefits. First, it provides the access of Li ions passing through grain boundaries with face conducting mode. Second, halide anions may diffuse to particle boundaries to decrease the bonding energy of LLZTO, similar to the mechanism of LiI in $Li_2S$-$P_2S_5$ [41]. Third, a favorable formability can be obtained to reduce the contact resistance of grain/grain and electrolyte/electrode [41]. The ionic conductivity of LiCl was also tested (Fig. S4). The value is as low as $1.1 \times 10^{-9}$ S/cm, which indicates that LiCl is not a good ionic conductor, in consistence with the results previously reported [42]. From these viewpoints, along with the comparable ionic conductivity for LiX-coated LLZTO regardless of the impurity phases, the improvement in solid electrolyte conductivity can be attributed to the LiX coating but neither to the pure solvents nor to the chemical change at interfaces.

Arrhenius plots of the total conductivity $\sigma$ in the temperature range from 25 to 80 °C are given in Fig. 5 for LiCl-doped LLZTO solid electrolytes prepared from ethanol and aqueous solutions. The inset displays Nyquist plots of the impedance at different temperatures. The ionic conductivities of LHE-LiCl are obviously higher than those of LHA-LiCl over the measured temperature range. The ionic conductivity of LHE-LiCl locates in the range from 0.56 mS/cm at 25 °C to 2.8 mS/cm at 80 °C. The impedance spectra for each temperature point are shown in the inset. The semicircles at high frequency region become smaller and are hardly to be observed at higher temperature points, indicating a negligible grain boundary contribution. The activation energy $E_a$ was determined from the slope of the linear Arrhenius plot using the equation: $\sigma = \sigma_0 \exp(-E_a/k_B T)$, where $\sigma_0$ is the pre-exponential parameter and $k_B$ is the Boltzmann constant. The activation energy is 0.28 eV for the sample prepared from the ethanol solution and is 0.39 eV for the sample prepared from the aqueous solution. The reduced activation energy may be attributed to a less impurity located on grain boundaries in the former sample.

Changes in impedance and mass of the LHE-LiCl-LLZTO electrolyte in the open air with time passing have been examined, as demonstrated in Fig. S5. Because of the strong water-absorption behavior, the presence of LiCl in LHE-LiCl-LLZTO leads to the difficulty for the test. Therefore, the testing apparatus is partially opened to limit the air exposure during testing. The total resistance (Fig. S5a) decreases with prolonging the exposing time until reaches a constant after 8 days, i.e., the conductivity of LHE-LiCl-LLZTO increases from 0.56 mS/cm to 12 mS/cm in the ambient atmosphere after 8 days. The decrease of resistance can be understood by the formation of $LiCl{\cdot}H_2O$ on the grain boundaries [48,49]. The mass of the sample (Fig. S5b) increases gradually with exposing time. This is expected for the formation of $LiCl{\cdot}H_2O$ on the grain boundary.

### *3.3. Structural and thermal properties of LiCl-coated LLZTO*

The chemical compositions of LHE-LiCl-LLZTO were evaluated using SEM-EDS performed on a fractured sample. EDS point analyses were carried out both on the grain and on the grain boundary to compare the elemental difference, as depicted in Fig. 6a. By comparing the atomic percentage (Fig. 6c) at the positions of EDS1 and EDS2, we see a significantly higher Cl content in the latter position than the former. Along with the EDS mapping data (Fig. 6d), we know that LiCl is homogeneously distributed on the grain boundaries and La, Zr, and Ta are homogeneously distributed in LLZTO grains. Fig. 6b schematically illustrates the LiCl-coated LLZTO sample.

The Raman spectra of the pristine LLZTO and the LHE-LiCl-LLZTO samples measured at the random points detect whether or not the garnet reacts with LiCl and ethanol. As shown in Fig. 7a, all peaks in both samples can be indexed to cubic LLZO [50], indicating a high purity of cubic garnet phase. In addition, no apparent difference between the two samples was observed, confirming no reaction between LLZTO with LiCl or ethanol. No Raman signal assigned to $Li_2CO_3$, appeared at 1088 $cm^{-1}$ [51], is detected for both samples, indicating no $Li_2CO_3$ impurity in the measured samples. These results are agreement with the XRD results. The peak at ~650 $cm^{-1}$ is related to the stretching of $ZrO_6$ octahedra [52] and the peak at ~750 $cm^{-1}$ is associated with Ta corresponding to the stretching of $TaO_6$ octahedron [53,54]. For LHA-LiBr and LHA-LiI, additional Raman characteristic peaks regarding impurities should appear since impurity phases are clearly shown in the XRD patterns (Fig. 1).

The residual water and ethanol may deteriorate the performance of the garnet solid electrolyte. The thermal evolution is important so the TG measurements were performed on LHE-LiCl-LLZTO and compared with pristine LLZTO, as shown in Fig. 7b. Both samples show a broad endothermic peak at 200 °C, which can be attributed to the removal of $H_2O$ inserted in the crystalline lattice. It was suggested that the water molecules not only are adsorbed at the surface but also enter into the crystalline lattice [55]. However, the weight loss of LHE-LiCl-LLZTO (0.37%) at 200 °C is slightly higher than that of pristine LLZTO (0.25%). We speculate it is related to a trace of moisture in LiCl. Compared with pristine LLZTO, an additional weight loss in LHE-LiCl-LLZTO before 100 °C was detected. This may be associated with the residual ethanol solution absorbed on grain boundaries.

### *3.4. Electrochemical performance*

The shear modulus and Young's modulus of LiCl crystal are estimated to be slightly larger than 15 and 38 GPa, respectively, referring to those of LiI and LiBr [41]. A high shear modulus may be beneficial to suppress Li dendrite [56]. The Young's modulus of LiCl is lower than LLZO (150 GPa) [41], which is beneficial to sustain the

volume change during battery cycling [57]. LiCl-coated LLZTO may possess these merits.

Galvanostatic cycling tests were performed on Li/LHE-LiCl-LLZTO/Li and Li/PCL/LHE-LiCl-LLZTO/PCL/Li symmetric cells at a constant current density of 0.1 mA/cm$^2$. The Li/LHE-LiCl-LLZTO/Li symmetric cells were cycled at room temperature (Fig. S6a) and at 40 °C (Fig. S6b). The overpotential for both cells (Fig. S6) increased immediately over 5 V at initial current loading (0.1 mA/cm$^2$) regardless of the testing temperature. Kotobuki et al. reported similar behavior that the voltage drastically increased after polarization of Li/LLZO/Li cell for 70 s at a current density of 0.05 mA/cm$^2$ [58]. Such large polarization during stripping/plating indicates an incompatible behavior between LiCl-coated LLZTO and metallic Li such as, the poor contact wettability and lack of interphase between Li and garnet, leading to accumulation of large current at interfacial points/regions [59]. The residual solvent may deteriorate the stability as well. Our previous study reveals that PCL is stable toward metallic Li but cannot sustain Li dendrite at certain current density. For details please refers to Ref [28]. PCL films were thus used to separate the solid electrolyte from Li to construct Li/PCL/LHE-LiCl-LLZTO/PCL/Li cell (Fig. 8a). With PCL separation, good cycling stability (Fig. 8a) is achieved on the symmetric cell at room temperature. This indicates that $Li^+$ can transport through the electrolyte without degradation of LLZTO; and LiCl-coated LLZTO without high temperature sintering can effectively suppress Li dendrite under measured conditions. Short circuit, occurred in a Li/Au/LLZO/Au/Li symmetric cell because of Li dendrite penetration through pores and grain boundaries [60], is not observed in Li/PCL/LHE-LiCl-LLZTO/PCL/Li cell cycled over 100 h. Since the short circuit is impacted by the pores [60,61], the grain boundary modification in LiCl-coated LLZTO is beneficial to the dendrite suppression. Although it is a great challenge to completely stop the growth of lithium dendrite inside the solid electrolyte, LiCl coating improves the ability of LLZTO to prevent Li dendrite.

The Li/PCL/LHE-LiCl-LLZTO/PCL/Li symmetric cell was detached after cycling test. Many black spots (not shown here) were seen on the surface of Li electrode by eyes. The cross-section microstructure of LHE-LiCl-LLZTO after polarization loading was observed using SEM. Two sides of the electrolyte pellet contacted with Li are dark and the middle part of the pellet is grey (not shown here), confirming the incompatible behavior of LLZTO/Li. This is different from a short-circuited LLZO, in which the dark area penetrates through the pellet [60]. Fig. 8b shows a dark granule with a round shape grown inside the pellet, which is totally different from the morphology of the surrounding particles. Unfortunately, we cannot affirm the composition of the granule at present. We will try to detect it using focused ion beam along with electron energy loss spectroscopy in future work.

The oxidation potential of LiCl was calculated to be 4.2 V in literature [62]. No redox peak is observed from the CV curve (Fig. S7) tested on a In/LiCl/Li cell in the voltage range of −2.5−5 V. Therefore, LiX-coated LLZTO solid electrolyte is applicable to batteries with oxide cathodes. Fig. 8c shows the charge-discharge curves of the $LiFePO_4$/LHE-LiCl-LLZTO/Li cell at a current density of 0.03 mA/cm$^2$ between 2.55 and 4.2 V at ambient temperature (16 °C). The charging and discharging voltage plateaus started at 3.57 V and 3.28 V, respectively. The overpotential is larger than a typical $LiFePO_4$ cell based on the liquid electrolyte. In addition, the fluctuation indicates an instable interface between electrolyte and electrodes. A larger current density leads to a higher overpotential, as shown in Ref. [58]. Therefore, the battery can work for several cycles at a low current density of 0.03 mA/cm$^2$. However, due to the large interfacial resistance between the electrolyte and Li metal, the $LiFePO_4$/LHE-LiCl-LLZTO/Li cell shows a poor cycling stability. Figs. S8a and b show the cycling performance and the impedance spectra before and after cycling for the $LiFePO_4$/LHE-LiCl-LLZTO/Li cell, respectively. The specific capacity slowly decreases in the first 3 cycles. From the 4th cycle, the capacity sharply drops to near zero, which is mainly induced by intensively increased interfacial resistance between solid electrolyte and Li. This indicates large polarization still occurs even at a current density as low as 0.03 mA/cm$^2$. The EIS measurements (Fig. S8b) show that the interfacial resistance of electrolyte/Li (at the low frequency region) after cycling is one order of magnitude larger than that before cycling, in consistence with the result of the galvanostatic cycling tests on the symmetric cell.

As a comparison, a $LiFePO_4$/LHE-LiCl-LLZTO/Li battery without commercial liquid electrolyte added to the cathode side was tested. Due to the rigid nature of the oxide electrolyte, the contact between the cathode and the electrolyte is severely deteriorated by removing liquid electrolyte. The battery delivers almost zero capacity, as shown in Fig. S9, indicating that interfacial modification is also important the cathode side.

The cycling performance of the $LiFePO_4$/LHE-LiCl-LLZTO/PCL/Li cell is shown in Fig. S10. Compared to the cell without PCL buffer layer, the cell with PCL exhibits good cycling stability, indicating that interfacial modification plays a critical role on electrochemical performance for LLZO-based all-solid-state batteries. Future experiments will focus on improving the interfacial stability by designing various coating compounds and optimizing coating processes.

## 4. Conclusions

In summary, we have designed and prepared a new type of LiX-coated LLZTO hybrid solid electrolytes with solution method by using pre-synthesized Al and Ta co-doped LLZO at 900 °C. Although this sintering temperature is lower than that commonly used (over 1100 °C), a single LLZTO phase with cubic structure is obtained. LiX coating was prepared by evaporating a solvent at 160 °C from LiX-dissolved aqueous or ethanol solutions, though a trace (0.63 wt%) of solvent is detected. LiX is stable toward LLZTO without side reaction. LiX coating forms a consecutive layer by submerging the grain boundaries in LLZTO and thus increasing the relative density, improving the formability, as well as altering the ion transport from point to face conduction. By optimizing halogens in LiX and the coating concentration, we found that the LiCl-coated LLZTO sample prepared from a 6 wt% LiCl ethanol solution achieves the highest ionic conductivity of 0.56 mS/cm and low activation energy of 0.28 eV. Ethanol is superior to aqueous used as a solvent due to the higher purity phase observed from XRD, higher ionic conductivity and lower activation energy. The ionic conductivity for all LiX-coated samples is over 0.1 mS/cm, three orders of magnitude higher than pristine LLZTO ($4 \times 10^{-4}$ mS/cm), despite of the impurity phases in LiX-coated LLZTO. The significant enhancement of the ion transport is contributed by the intensively reduced grain boundary resistance by LiX coating. $LiFePO_4$/Li cells can well run based on LiCl-coated LLZTO solid electrolyte. This coating strategy for intergrain architecture engineering provides a new way for ceramic solid electrolytes to avoid high temperature sintering and might be used to improve the wettability of garnet-type solid electrolyte toward molten Li.

## Acknowledgments

This work was supported by the Science Foundation of Hebei Education Department (ZD2016033) and Natural Science Foundation of Hebei Province (E2018203301).

## Appendix A. Supplementary data

Supplementary data related to this article can be found at https://doi.org/10.1016/j.electacta.2018.08.079.

## References

[1] J.C. Bachman, S. Muy, A. Grimaud, H.H. Chang, N. Pour, S.F. Lux, O. Paschos, F. Maglia, S. Lupart, P. Lamp, L. Giordano, S.-H. Yang, Inorganic Solid-State electrolytes for lithium batteries: mechanisms and properties governing ion conduction, Chem. Rev. 116 (2016) 140–162.

[2] B. Zheng, H. Wang, J. Ma, Z. Gong, Y. Yang, A review of inorganic solid electrolyte/electrode interface in all-solid-state lithium batteries, Sci. Sin. Chim. 47 (2017) 579–593.

[3] R. Chen, W. Qu, X. Guo, L. Li, F. Wu, The pursuit of solid-state electrolytes for lithium batteries: from comprehensive insight to emerging horizons, Mater. Horiz. 3 (2016) 487–516.

[4] K. Kerman, A. Luntz, V. Viswanathan, Y.-M. Chiang, Z. Chen, Review—practical challenges hindering the development of solid state li ion batteries, J. Electrochem. Soc. 164 (2017) A1731–A1744.

[5] C. Sun, J. Liu, Y. Gong, D.P. Wilkinson, J. Zhang, Recent advances in all-solid-state rechargeable lithium batteries, Nano Energy 33 (2017) 363–386.

[6] X. Yao, B. Huang, J. Yin, G. Peng, Z. Huang, C. Gao, D. Liu, X. Xu, All-solid-state lithium batteries with inorganic solid electrolytes: review of fundamental science, Chin. Phys. B 25 (2016), 018802.

[7] B. Zhang, R. Tan, L. Yang, J. Zheng, K. Zhang, S. Mo, Z. Lin, F. Pan, Mechanisms and properties of ion-transport in inorganic solid electrolytes, Energy Storage Mater. 10 (2018) 139–159.

[8] R. Murugan, V. Thangadurai, W. Weppner, Fast lithium ion conduction in garnet-type $Li_7La_3Zr_2O_{12}$, Angew. Chem. 46 (2007) 7778–7781.

[9] H. Duan, H. Zheng, Y. Zhou, B. Xu, H. Liu, Stability of garnet-type Li ion conductors: an overview, Solid State Ionics (2018) https://doi.org/10.1016/j.ssi.2017.09.018.

[10] S. Ramakumar, C. Deviannapoorani, L. Dhivya, L.S. Shankar, R. Murugan, Lithium garnets: synthesis, structure, $Li^+$ conductivity, $Li^+$ dynamics and applications, Prog. Mater. Sci. 88 (2017) 325–411.

[11] Y. Ren, K. Chen, R. Chen, T. Liu, Y. Zhang, C.-W. Nan, B. Vyas, Oxide electrolytes for lithium batteries, J. Am. Ceram. Soc. 98 (2015) 3603–3623.

[12] V. Thangadurai, S. Narayanan, D. Pinzaru, Garnet-type solid-state fast Li ion conductors for Li batteries: critical review, Chem. Soc. Rev. 43 (2014) 4714–4727.

[13] Y. Jin, P.J. Mcginn, Al-doped $Li_7La_3Zr_2O_{12}$ synthesized by a polymerized complex method, J. Power Sources 196 (2011) 8683–8687.

[14] T. Thompson, A. Sharafi, M.D. Johannes, A. Huq, J.L. Allen, J. Wolfenstine, J. Sakamoto, A tale of two sites: on defining the Carrier concentration in garnet-based ionic conductors for advanced Li batteries, Adv. Energy Mater. 5 (2015), 1500096.

[15] J. Awaka, N. Kijima, H. Hayakawa, J. Akimoto, Synthesis and structure analysis of tetragonal $Li_7La_3Zr_2O_{12}$ with the garnet-related type structure, J. Solid State Chem. 182 (2009) 2046–2052.

[16] J. Awaka, A. Takashima, H. Hayakawa, N. Kijima, Y. Idemoto, J. Akimoto, Single crystal synthesis of cubic garnet related-type $Li_7La_3Zr_2O_{12}$ by a self-flux method, Key Eng. Mater. 485 (2011) 99–102.

[17] J.L. Allen, J. Wolfenstine, E. Rangasamy, J. Sakamoto, Effect of substitution (Ta, Al, Ga) on the conductivity of $Li_7La_3Zr_2O_{12}$, J. Power Sources 206 (2012) 315–319.

[18] L. Buannic, B. Orayech, J.-M. López Del Amo, J. Carrasco, N.A. Katcho, F. Aguesse, W. Manalastas, W. Zhang, J. Kilner, A. Llordés, Dual substitution strategy to enhance Li+ ionic conductivity in $Li_7La_3Zr_2O_{12}$ solid electrolyte, Chem. Mater. 29 (2017) 1769–1778.

[19] K. Fu, Y. Gong, B. Liu, Y. Zhu, S. Xu, Y. Yao, L. Wei, C. Wang, S.D. Lacey, J. Dai, Toward garnet electrolyte–based Li metal batteries: an ultrathin, highly effective, artificial solid-state electrolyte/metallic Li interface, Sci. Adv. 3 (2017), e1601659.

[20] C. Chen, S. Ling, X. Guo, H. Li, Space charge layer effect in rechargeable solid state lithium batteries: principle and perspective, Energy Storage Sci. Technol. 5 (2016) 668–677.

[21] H. Kähäri, M. Teirikangas, J. Juuti, H. Jantunen, N. Alford, Dielectric properties of lithium molybdate ceramic fabricated at room temperature, J. Am. Ceram. Soc. 97 (2014) 3378–3379.

[22] J. Guo, H. Guo, A.L. Baker, M.T. Lanagan, E.R. Kupp, G.L. Messing, C.A. Randall, Cold sintering: a paradigm shift for processing and integration of ceramics, Angew. Chem. 55 (2016) 11457–11461.

[23] S.S. Berbano, J. Guo, H. Guo, M.T. Lanagan, C.A. Randall, Cold sintering process of $Li_{1.5}Al_{0.5}Ge_{1.5}(PO_4)_3$ solid electrolyte, J. Am. Ceram. Soc. 100 (2017) 2123–2135.

[24] V. Thangadurai, W. Weppner, $Li_6ALa_2Ta_2O_{12}$ (A = Sr, Ba): novel garnet-like oxides for fast lithium ion conduction, Adv. Funct. Mater. 15 (2005) 107–112.

[25] R. Jalem, Y. Yamamoto, H. Shiiba, M. Nakayama, H. Munakata, T. Kasuga, K. Kanamura, Concerted migration mechanism in the Li ion dynamics of garnet-type $Li_7La_3Zr_2O_{12}$, Chem. Mater. 25 (2013) 425–430.

[26] Y. Li, Z. Wang, C. Li, Y. Cao, X. Guo, Densification and ionic-conduction improvement of lithium garnet solid electrolytes by flowing oxygen sintering, J. Power Sources 248 (2014) 642–646.

[27] W. Xia, B. Xu, H. Duan, Y. Guo, H. Kang, H. Li, H. Liu, Ionic conductivity and air stability of Al-doped $Li_7La_3Zr_2O_{12}$ sintered in alumina and pt crucibles, ACS Appl. Mater. Interfaces 8 (2016) 5335–5342.

[28] D. Zhang, L. Zhang, K. Yang, H. Wang, C. Yu, D. Xu, B. Xu, L.-M. Wang, Superior blends solid polymer electrolyte with integrated hierarchical architectures for all-solid-state lithium-ion batteries, ACS Appl. Mater. Interfaces 9 (2017) 36886–36896.

[29] X. Han, Y. Gong, K.K. Fu, X. He, G.T. Hitz, J. Dai, A. Pearse, B. Liu, H. Wang, G. Rubloff, Negating interfacial impedance in garnet-based solid-state Li metal batteries, Nat. Mater. 16 (2017) 572.

[30] F. Han, J. Yue, X. Zhu, C. Wang, Suppressing Li dendrite formation in $Li_2S$-$P_2S_5$ solid electrolyte by LiI incorporation, Adv. Energy Mater. (2018), 1703644.

[31] K. Ishiguro, Y. Nakata, M. Matsui, I. Uechi, Y. Takeda, O. Yamamoto, N. Imanishi, Stability of Nb-doped cubic $Li_7La_3Zr_2O_{12}$ with lithium metal, J. Electrochem. Soc. 160 (2013) A1690–A1693.

[32] S. Narayanan, F. Ramezanipour, V. Thangadurai, Dopant concentration-porosity-Li-ion conductivity relationship in garnet-type $Li_{5+2x}La_3Ta_{2-x}Y_xO_{12}$ (0.05 </= x </= 0.75) and their stability in water and 1 M LiCl, Inorg. Chem. 54 (2015) 6968–6977.

[33] Y. Shimonishi, A. Toda, T. Zhang, A. Hirano, N. Imanishi, O. Yamamoto, Y. Takeda, Synthesis of garnet-type $Li_{7-x}La_3Zr_2O_{12-1/2x}$ and its stability in aqueous solutions, Solid State Ionics 183 (2011) 48–53.

[34] Y. Wang, W. Lai, Phase transition in lithium garnet oxide ionic conductors $Li_7La_3Zr_2O_{12}$: the role of Ta substitution and $H_2O/CO_2$ exposure, J. Power Sources 275 (2015) 612–620.

[35] C. Galven, J.-L. Fourquet, M.-P. Crosnier-Lopez, F.o. Le Berre, Instability of the lithium garnet $Li_7La_3Sn_2O_{12}$: $Li^+/H^+$ exchange and structural study, Chem. Mater. 23 (2011) 1892–1900.

[36] M. Nyman, T.M. Alam, S.K. McIntyre, G.C. Bleier, D. Ingersoll, Alternative approach to increasing li mobility in Li-La-Nb/Ta garnet electrolytes, Chem. Mater. 22 (2010) 5401–5410.

[37] A. Sharafi, S. Yu, M. Naguib, M. Lee, C. Ma, H.M. Meyer, J. Nanda, M. Chi, D.J. Siegel, J. Sakamoto, Impact of air exposure and surface chemistry on Li–$Li_7La_3Zr_2O_{12}$ interfacial resistance, J. Mater. Chem. A 5 (2017) 13475–13487.

[38] Y. Li, Z. Wang, Y. Cao, F. Du, C. Chen, Z. Cui, X. Guo, W-Doped $Li_7La_3Zr_2O_{12}$ ceramic electrolytes for solid state Li-ion batteries, Electrochim. Acta 180 (2015) 37–42.

[39] L. Zhang, K. Yang, J. Mi, L. Lu, L. Zhao, L. Wang, Y. Li, H. Zeng, $Na_3PSe_4$: a novel chalcogenide solid electrolyte with high ionic conductivity, Adv. Energy Mater. 5 (2015), 1501294.

[40] L. Zhang, D. Zhang, K. Yang, X. Yan, L. Wang, J. Mi, B. Xu, Y. Li, Vacancy-contained tetragonal $Na_3SbS_4$ superionic conductor, Adv. Sci. 3 (2016), 1600089.

[41] A. Kato, M. Yamamoto, A. Sakuda, A. Hayashi, M. Tatsumisago, Mechanical properties of $Li_2S$–$P_2S_5$ glasses with lithium halides and application in all-solid-state batteries, ACS Appl. Energy Mater. 1 (2018) 1002–1007.

[42] X. Liang, Q. Pang, I.R. Kochetkov, M.S. Sempere, H. Huang, X. Sun, L.F. Nazar, A facile surface chemistry route to a stabilized lithium metal anode, Nat. Energy. 2 (2017) 17119.

[43] Y. Li, B. Xu, H. Xu, H. Duan, X. Lu, S. Xin, W. Zhou, L. Xue, G. Fu, A. Manthiram, J.B. Goodenough, Hybrid polymer/garnet electrolyte with a small interfacial resistance for lithium-ion batteries, Angew. Chem. 56 (2017) 753–756.

[44] J. Yan, J. Yu, B. Ding, Mixed ionic and electronic conductor for Li-metal anode protection, Adv. Mater. 30 (2018), 1705105.

[45] A. Zhou, Q. Liu, Y. Wang, W. Wang, X. Yao, W. Hu, L. Zhang, X. Yu, J. Li, H. Li, $Al_2O_3$ surface coating on $LiCoO_2$ through a facile and scalable wet-chemical method towards high-energy cathode materials withstanding high cutoff voltages, J. Mater. Chem. A 5 (2017) 24361–24370.
[46] M. Yoshizawa, M. Hirao, K. Ito-Akita, H. Ohno, Ion conduction in zwitterionic-type molten salts and their polymers, J. Mater. Chem. 11 (2001) 1057–1062.
[47] Y. Li, Y. Cao, X. Guo, Influence of lithium oxide additives on densification and ionic conductivity of garnet-type $Li_{6.75}La_3Zr_{1.75}Ta_{0.25}O_{12}$ solid electrolytes, Solid State Ionics 253 (2013) 76–80.
[48] N. Imanishi, M. Matsui, Y. Takeda, O. Yamamoto, Lithium ion conducting solid electrolytes for aqueous lithium-air batteries, Electrochemistry 82 (2014) 938–945.
[49] K. Takahashi, J. Ohmura, D. Im, D.J. Lee, T. Zhang, N. Imanishi, A. Hirano, M.B. Phillipps, Y. Takeda, O. Yamamoto, A super high lithium ion conducting solid electrolyte of grain boundary modified $Li_{1.4}Ti_{1.6}Al_{0.4}(PO_4)_3$, J. Electrochem. Soc. 159 (2012) A342–A348.
[50] F. Tietz, T. Wegener, M.T. Gerhards, M. Giarola, G. Mariotto, Synthesis and Raman micro-spectroscopy investigation of $Li_7La_3Zr_2O_{12}$, Solid State Ionics 230 (2013) 77–82.
[51] W. Xia, B. Xu, H. Duan, X. Tang, Y. Guo, H. Kang, H. Li, H. Liu, Reaction mechanisms of lithium garnet pellets in ambient air: the effect of humidity and $CO_2$, J. Am. Ceram. Soc. 100 (2017) 2832–2839.
[52] D. Rettenwander, A. Welzl, L. Cheng, J. Fleig, M. Musso, E. Suard, M.M. Doeff, G.J. Redhammer, G. Amthauer, Synthesis, crystal chemistry, and electrochemical properties of $Li_{7-2x}La_3Zr_{2-x}Mo_xO_{12}$ (x = 0.1-0.4): stabilization of the cubic garnet polymorph via substitution of $Zr^{4+}$ by $Mo^{6+}$, Inorg. Chem. 54 (2015) 10440–10449.
[53] L. Cheng, C.H. Wu, A. Jarry, W. Chen, Y. Ye, J. Zhu, R. Kostecki, K. Persson, J. Guo, M. Salmeron, G. Chen, M. Doeff, Interrelationships among grain size, surface composition, air stability, and interfacial resistance of Al-substituted $Li_7La_3Zr_2O_{12}$ solid electrolytes, ACS Appl. Mater. Interfaces 7 (2015) 17649–17655.
[54] T. Thompson, J. Wolfenstine, J.L. Allen, M. Johannes, A. Huq, I.N. David, J. Sakamoto, Tetragonal vs. cubic phase stability in Al – free Ta doped $Li_7La_3Zr_2O_{12}$ (LLZO), J. Mater. Chem. A 2 (2014) 13431–13436.
[55] G. Larraz, A. Orera, M.L. Sanjuán, Cubic phases of garnet-type $Li_7La_3Zr_2O_{12}$: the role of hydration, J. Mater. Chem. A 1 (2013) 11419–11428.
[56] C. Monroe, J. Newman, The impact of elastic deformation on deposition kinetics at lithium/polymer interfaces, J. Electrochem. Soc. 152 (2005) A396–A404.
[57] A. Sakuda, A. Hayashi, M. Tatsumisago, Sulfide solid electrolyte with favorable mechanical property for all-solid-state lithium battery, Sci. Rep. 3 (2013) 2261.
[58] M. Kotobuki, H. Munakata, K. Kanamura, Y. Sato, T. Yoshida, Compatibility of $Li_7La_3Zr_2O_{12}$ solid electrolyte to all-solid-state battery using Li metal anode, J. Electrochem. Soc. 157 (2010) A1076–A1079.
[59] K. Fu, Y. Gong, B. Liu, Y. Zhu, S. Xu, Y. Yao, W. Luo, C. Wang, S.D. Lacey, J. Dai, Y. Chen, Y. Mo, E. Wachsman, L. Hu, Toward garnet electrolyte–based Li metal batteries: an ultrathin, highly effective, artificial solid-state electrolyte/metallic Li interface, Sci. Adv. 3 (2017), e1601659.
[60] K. Park, B.-C. Yu, J.-W. Jung, Y. Li, W. Zhou, H. Gao, S. Son, J.B. Goodenough, Electrochemical nature of the cathode interface for a solid-state lithium-ion battery: interface between $LiCoO_2$ and garnet-$Li_7La_3Zr_2O_{12}$, Chem. Mater. 28 (2016) 8051–8059.
[61] Y. Ren, Y. Shen, Y. Lin, C.-W. Nan, Direct observation of lithium dendrites inside garnet-type lithium-ion solid electrolyte, Electrochem. Commun. 57 (2015) 27–30.
[62] Y. Zhu, X. He, Y. Mo, Origin of outstanding stability in the lithium solid electrolyte materials: insights from thermodynamic analyses based on first-principles calculations, ACS Appl. Mater. Interfaces 7 (2015) 23685–23693.